# Supplementary Information

## Ambient scalable fabrication of high-performance flexible perovskite solar cells

Pengchi Liu[†1], Hui Wang[†2,4], Tianqi Niu[†1], Lei Yin[1], Yachao Du[1], Lei Lang[1], Zheng Zhang[1], Yongchao Tu[1], Xiujie Liu[1], Xin Chen[1], Shuang Wang[1], Nan Wu[1], Ru Qin[1], Likun Wang[2], Shaoan Yang[2], Chunfu Zhang[4], Xu Pan[5], Shengzhong (Frank) Liu[1,2,3], Kui Zhao[1,*]

[1]Key Laboratory of Applied Surface and Colloid Chemistry, National Ministry of Education; Shaanxi Key Laboratory for Advanced Energy Devices. Shaanxi Engineering Lab for Advanced Energy Technology, School of Materials Science and Engineering, Shaanxi Normal University, Xi'an 710119, P. R. China.

[2]Key Laboratory of Photoelectric Conversion and Utilization of Solar Energy, Dalian Institute of Chemical Physics, Chinese Academy of Sciences, Dalian, 116023, Liaoning, China;

[3]Center of Materials Science and Optoelectronics Engineering, University of Chinese Academy of Sciences, Beijing, 100049, P. R. China.

[4]Wide Bandgap Semiconductor Technology Disciplines State Key Laboratory, Shaanxi Joint Key Laboratory of Graphene, School of Microelectronics, Xidian University, Xi'an 710071, China.

[5]Key Laboratory of Photovoltaic and Energy Conservation Material, Institute of Solid-State Physics 8 (ISSP), Hefei Institutes of Physical Science (HIPS), Chinese Academy of Sciences, Hefei 230031, China.

[†] These authors contributed equally.

* Email: zhaok@snnu.edu.cn

## Experimental Section

***Materials***: Formamidine iodide (FAI, ≥99.9%), cesium bromide (CsBr, 98%), methylammonium chloride (MACl, ≥99.9%), Pb (II) iodide ($PbI_2$, ≥99.99%) and 2,2',7,7'-tetrakis(N,N'-di-p-methoxyphenylamine)-9,9'-spirobifluorene (Spiro-OMeTAD) were purchased from Advanced Election Technology Co., Ltd. Ionic liquid 1-butyl-3-methylimidazolium thiocyanate (BPySCN) was brought from Xi'an Polymer Light Technology Cory Co., Ltd. N, N-dimethylformamide (DMF, 99.8%) and N-Methylpyrrolidone (NMP, ≥99.9%) were obtained from Alfa Aesar. 4-tert-butylpyridine (t-BP, 99%) and lithiumbis(trifluoromethylsulfonyl)imide salt (LiTFSI) were purchased from Sigma-Aldrich. Chlorobenzene (CB, 99.5%) and isopropanol (IPA, 99.5%) were purchased from China National Pharmaceutical Group Corporation. $SnO_2$ colloid precursor (tin (iv) oxide, 15% in $H_2O$ colloidal dispersion) was obtained from Alfa Aesar. All chemicals were applied as received without further purification.

***Precursor solution preparation.*** $SnO_2$ colloidal precursor was diluted with deionized water with a ratio of 1:6. The $FA_{0.95}Cs_{0.05}PbI_3$ perovskite solution was prepared by dissolving 163.4 mg FAI, 462 mg $PbI_2$, 10.7 mg CsBr, 23.6 mg MACl and BPySCN under different concentrations in 100 μL NMP and 1mL DMF. The Spiro-OMeTAD solution was prepared by dissolving 90 mg Spiro-OMeTAD in 1 mL CB with 22 μL Li-TFSI solution (520 mg in 1 mL ACN), 20 μL Co-TFSI solution (375 mg Co-TFSI in 1 mL ACN) and 36 μL 4-tert-butylpyridine.

### Device fabrication

***Fabrication of small-area devices.*** Fluorine-doped tin oxide (FTO) glass substrates and indium tin oxide (ITO)-coated flexible PET substrates (ca. 50 μm thick) were cleaned by sequential sonication in a detergent, deionized water, and ethanol, then dried in ovens and treated with ozone plasma before blade-coating. The electron transport layer (ETL), perovskite layer, and hole transport layer (HTL) were all fabricated by blade-coating in ambient conditions. The $SnO_2$ ETL was fabricated by blade-coating the diluted solution on the pre-heated substrate at 40 °C at a speed of 20 mm/s and then annealed at 100 °C for 30 min. For the perovskite deposition process, the precursor solution was dropped onto a 40 °C pre-heated substrate and blade-coated at a speed of 20 mm/s. An airflow was applied to the as-casted films for several seconds to accelerate the evaporation of the solvent. Then, perovskite films were transferred to the hotplate and annealed at 100 °C for 15 min. After depositing the absorber layer, the 2-phenylethanamine hydroiodide (PEAI) layer was fabricated by printing the PEAI solution (5.0 mg/ml in IPA) on the 40 °C pre-heated perovskite layer at a speed of 25 mm/s. The HTL was deposited on the top of perovskite films by blade coating the Spiro-OMeTAD solution at a speed of 20 mm/s. Finally, the 80 nm gold electrode was thermally evaporated under vacuum. A non-refractive mask was employed to determine the active device area of 0.09 $cm^2$.

***Fabrication of flexible solar modules.*** The flexible solar module with 30 sub-cells was constructed by P1, P2, and P3 scribing lines with a wavelength of 1064 nm. The etched PET/ITO substrate was pre-patterned for P1 (ca. 200 μm width) and then cleaned with acetone and isopropanol to eliminate the adhesive residue. The subsequent processes for the preparation of $SnO_2$, perovskite, PEAI, and Spiro-OMeTAD layers are the same as the small-area device procedures. P2 and P3 scribing lines were patterned using a 355 nm picosecond laser scribing system (OpTek System, Inc., USA). The P2 lines (ca. 100 μm wide) were implemented with an average laser power of 12 W and a pulse repetition frequency of 65 kHz. After deposition of the gold electrode, the P3 lines (ca. 80 μm width) were patterned with an average laser power of 0.78 W and a pulse repetition frequency of 80 kHz. The distance interval between P1, P2, and P3 lines is ca. 30 μm. The active area of 117.7 $cm^2$ was determined by calculating the difference between the shadow mask and the dead zone.

***Material characterization.*** The morphology of perovskite films was evaluated by field emission scanning electron microscopy (SEM, Hitachi, SU-8020) and atomic force microscopy (AFM, Bruker Dimension Icon instrument). X-ray photoelectron spectroscopy (XPS) was analyzed by ESCALAB 250, Al Kα, Thermo Fisher Scientific. Fourier transform infrared (FTIR) spectroscopy was obtained using a Bruker Vertex 70 infrared spectrophotometer (FTIR, Bruker VERTEX 70). Dynamic light scattering (DLS) was conducted on NanoBrook 90 Plusplas. ToF-SIMS measurement was performed on a PHI nanoTOF II instrument. Steady-state photoluminescence (PL) and time-resolved photoluminescence (TRPL) were measured using a PicoQuant FT-300 spectrometer, with a 510 nm laser. Micro-PL mapping was measured by a laser scanning confocal microscope (Enlitech, SPCM-1000) with a 470 nm pulse laser, in which the signal of area 625 $\mu m^2$ was collected. UV-visible absorption was performed with a UV-visible spectrometer (PerkinElmer UV-Lambda 950). Ultraviolet photoelectron spectroscopy (UPS) was carried out on a monochromatic He I light source (21.22 eV) and a VG Scienta R4000 analyzer. X-ray diffraction (XRD) measurements were conducted using a DX-2700BH diffractometer. The grazing incidence X-ray diffraction (GIXRD) tests were realized by using a high-resolution X-ray Diffractometer (Smartlab (9), Japan). Grazing incidence wide-angle scattering (GIWAXS) at an incidence angle of 0.4° was performed at BL17B1 beamline of Shanghai Synchrotron Radiation Facility (SSRF) using the X-ray energy of 10 KeV. The measurement conditions of *in-situ* UV-vis absorption and *in-situ* PL spectroscopies were described previously as reference[16].

**Device characterization.**

The current density-voltage (*J–V*) characteristics of the devices were obtained by solar simulator equipment (Enlitech, SS-F5), and the illumination intensity (100 $mW \cdot cm^{-2}$, AM 1.5G) was calibrated via a reference silicon cell with a KG5 filter. The scan range was from 1.5 V to 0 V with a 0.02 V bias step and 20 ms delay time. The external quantum efficiency (EQE) was characterized by a QE-R system (Enli Technology Co., Ltd.) using a 300-WXe lamp as the light source. The impedance spectroscopic measurements (EIS) and capacitance-voltage (C–V) measurements were measured

using the electrochemical workstation (IM6ex, Zahner, Germany) in dark conditions. Transient photocurrent (TPC) measurement was carried out with a Paios 4.0 instrument (FLUXiM AG, Switzerland).

**Statistical Analysis**

All statistical analyses were performed with Origin 2023. The data obtained from J-V, , XPS, FTIR, $^{1}$H NMR, in situ PL, in situ UV-Vis, SEM, PL, PL mapping, UPS, C-V, MS and TPC were the original data. The other data were obtained by transferring the corresponding original data according to the calculation formula.Supporting information data including J-V, EQE, stabilized power output, UV-vis absorption, AFM, GIWAXs, GIXRD, UPS, dark I-V, XRD measurements, and certified reports for flexible module, and theoretical structures for DFT calculation.

**DFT calculation**

The Vienna Ab Initio Simulation Package (VASP) was utilized to conduct density functional theory (DFT) computations under the generalized gradient approximation (GGA) employing the Perdew-BurkeErnzerhof (PBE) formulation.[1] The ionic cores were described using projected augmented wave (PAW) potentials, while valence electrons were incorporated using a plane wave basis set with a kinetic energy cutoff of 400 eV.[2] The $FAPbI_3$ (100) surface models containing 3×3×2 supercells were constructed in the slab structure with a vacuum layer thickness of 15 Å to isolate the surface slab from its periodic duplicates. The equilibrium lattice constant of the cubic $FAPbI_3$ unit cell was optimized to be a=6.404 Å. During structural optimizations, the Γ point grid was employed for Brillouin zone integration. Self-consistency of electronic energy was attained when the energy change fell below $10^{-5}$ eV. Convergence of geometry optimization was achieved when the force change dropped below 0.02 eV/Å on each atom. The bottom stoichiometric layer was fixed to allow the top region to fully relax the $FAPbI_3$ crystal structure, including lattice parameters and internal atomic positions Grimme's DFT-D3 methodology was employed to account for dispersion interactions.[3] The adsorption energy (Eads) of additive was defined as $E_{ads}=E_{additive+surf}-E_{surf}-E_{additve}$, where $E_{additive+surf}$, $E_{surf}$, and $E_{additve}$ are the energy of additive adsorbed on the surface.

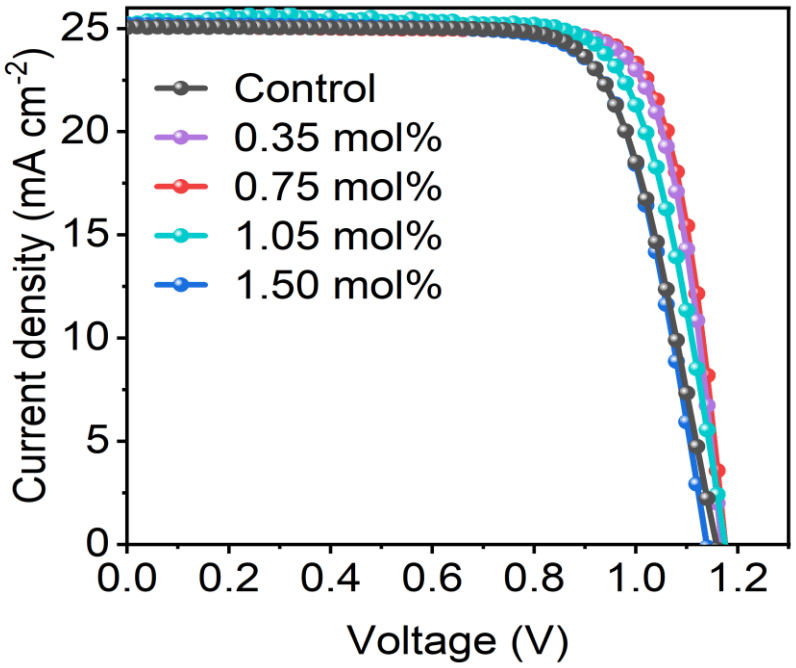


**Figure S1.** *J–V* curves of the champion rigid PSCs based on BPySCN under different injection concentrations.

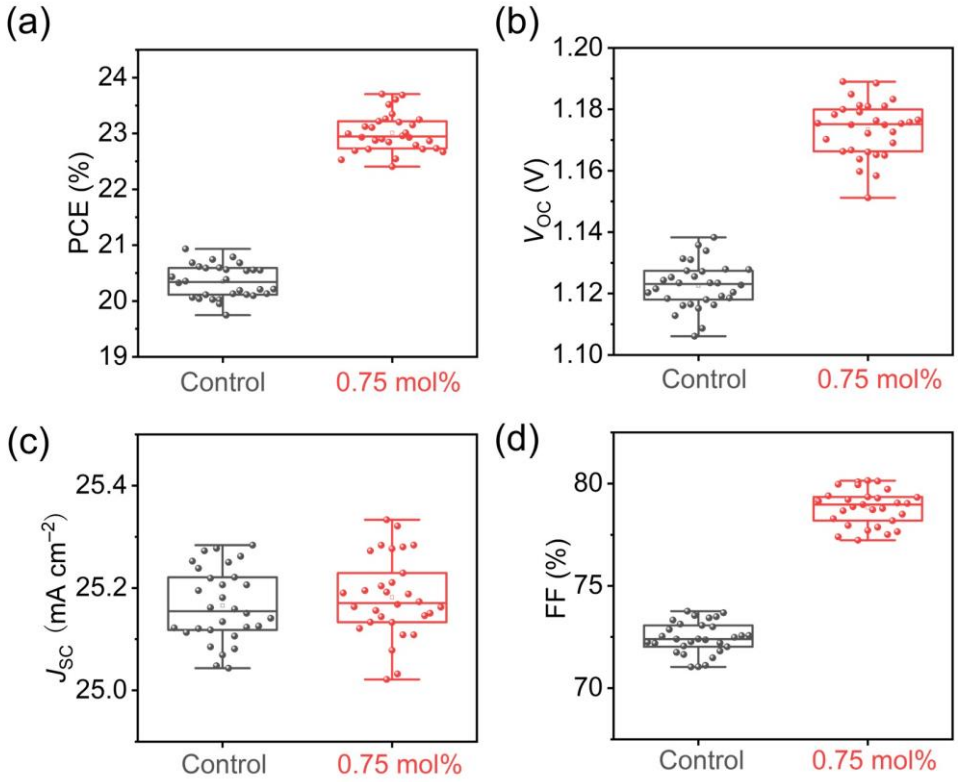


**Figure S2.** Statistical distribution of photovoltaic parameters of 30 individual devices in each case.

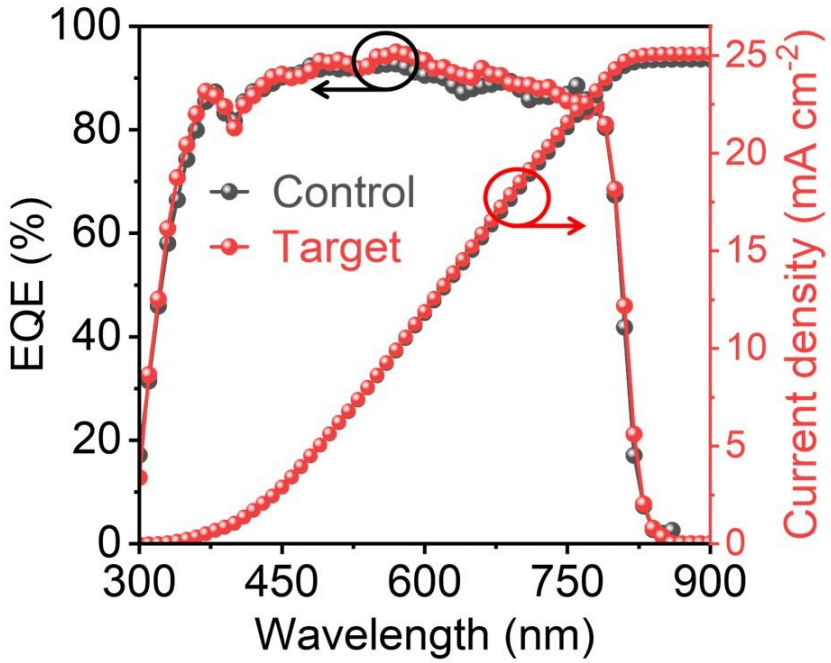


**Figure S3.** EQE curves and the corresponding integrated current density of champion rigid PSCs.

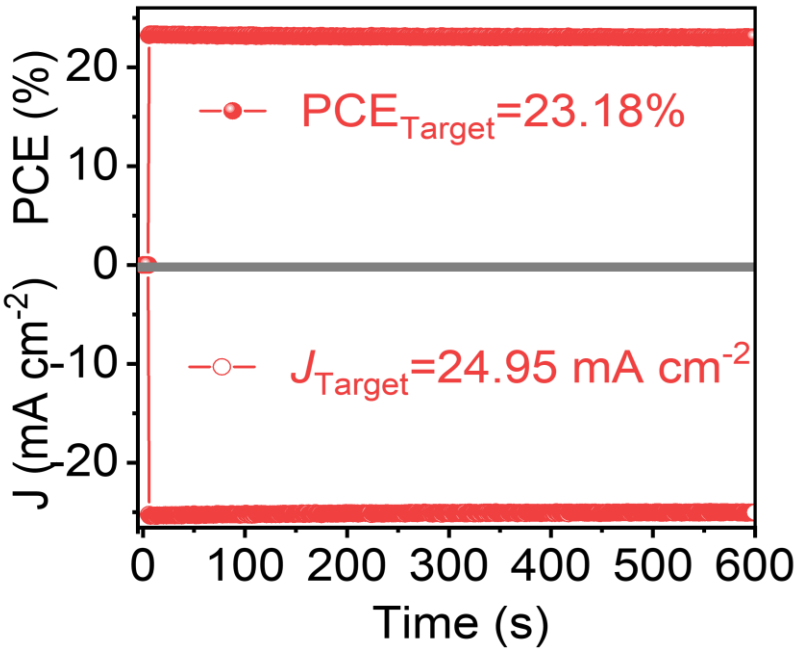


**Figure S4.** Stabilized power output of BPySCN-based champion rigid device measured at a fixed maximum power point (MPP) voltage as a function of time.

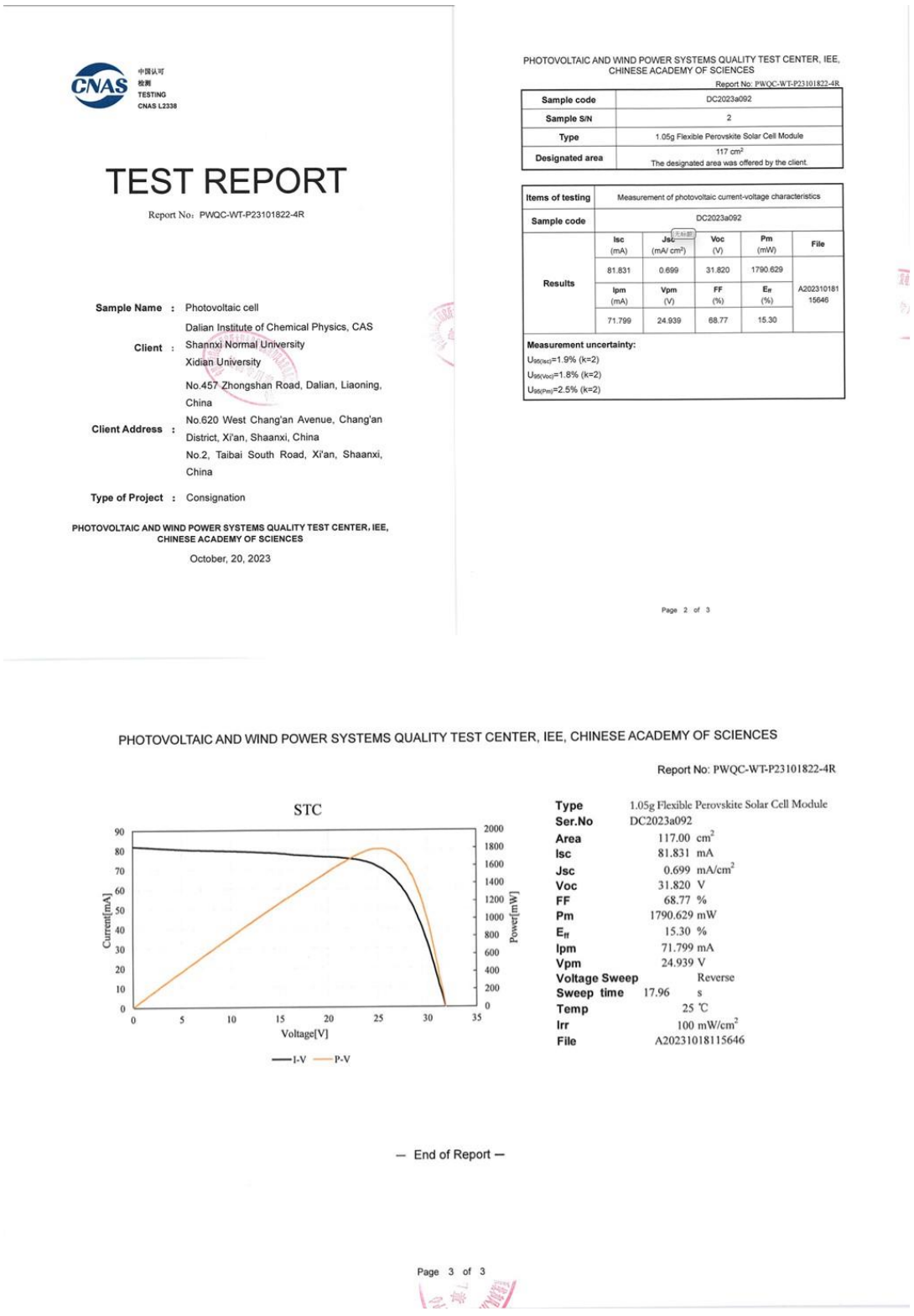

CNAS 中国认可 检测 TESTING CNAS L2338

# TEST REPORT

Report No: PWQC-WT-P23101822-4R

**Sample Name :** Photovoltaic cell

**Client :** Dalian Institute of Chemical Physics, CAS
Shannxi Normal University
Xidian University

**Client Address :** No.457 Zhongshan Road, Dalian, Liaoning, China
No.620 West Chang'an Avenue, Chang'an District, Xi'an, Shaanxi, China
No.2, Taibai South Road, Xi'an, Shaanxi, China

**Type of Project :** Consignation

**PHOTOVOLTAIC AND WIND POWER SYSTEMS QUALITY TEST CENTER, IEE, CHINESE ACADEMY OF SCIENCES**

October, 20, 2023

PHOTOVOLTAIC AND WIND POWER SYSTEMS QUALITY TEST CENTER, IEE, CHINESE ACADEMY OF SCIENCES

Report No: PWQC-WT-P23101822-4R

| | |
|---|---|
| **Sample code** | DC2023a092 |
| **Sample S/N** | 2 |
| **Type** | 1.05g Flexible Perovskite Solar Cell Module |
| **Designated area** | 117 $cm^2$ The designated area was offered by the client. |

| **Items of testing** | Measurement of photovoltaic current-voltage characteristics | | | | |
|---|---|---|---|---|---|
| **Sample code** | DC2023a092 | | | | |
| **Results** | **Isc** (mA) | **Jsc** (mA/ $cm^2$) | **Voc** (V) | **Pm** (mW) | **File** |
| | 81.831 | 0.699 | 31.820 | 1790.629 | A202310181 15646 |
| | **Ipm** (mA) | **Vpm** (V) | **FF** (%) | **Eff** (%) | |
| | 71.799 | 24.939 | 68.77 | 15.30 | |

**Measurement uncertainty:**
$U_{95(Isc)}$=1.9% (k=2)
$U_{95(Voc)}$=1.8% (k=2)
$U_{95(Pm)}$=2.5% (k=2)

Page 2 of 3

PHOTOVOLTAIC AND WIND POWER SYSTEMS QUALITY TEST CENTER, IEE, CHINESE ACADEMY OF SCIENCES

Report No: PWQC-WT-P23101822-4R




| | |
|---|---|
| **Type** | 1.05g Flexible Perovskite Solar Cell Module |
| **Ser.No** | DC2023a092 |
| **Area** | 117.00 $cm^2$ |
| **Isc** | 81.831 mA |
| **Jsc** | 0.699 $mA/cm^2$ |
| **Voc** | 31.820 V |
| **FF** | 68.77 % |
| **Pm** | 1790.629 mW |
| **$E_{ff}$** | 15.30 % |
| **Ipm** | 71.799 mA |
| **Vpm** | 24.939 V |
| **Voltage Sweep** | Reverse |
| **Sweep time** | 17.96 s |
| **Temp** | 25 ℃ |
| **Irr** | 100 $mW/cm^2$ |
| **File** | A20231018115646 |

— End of Report —

Page 3 of 3

**Figure S5.** Certified reports for the 117.0 $cm^2$ flexible perovskite solar module by Chinese photovoltaic and Wind Power Systems Quality Test Center (PWQTC, China).

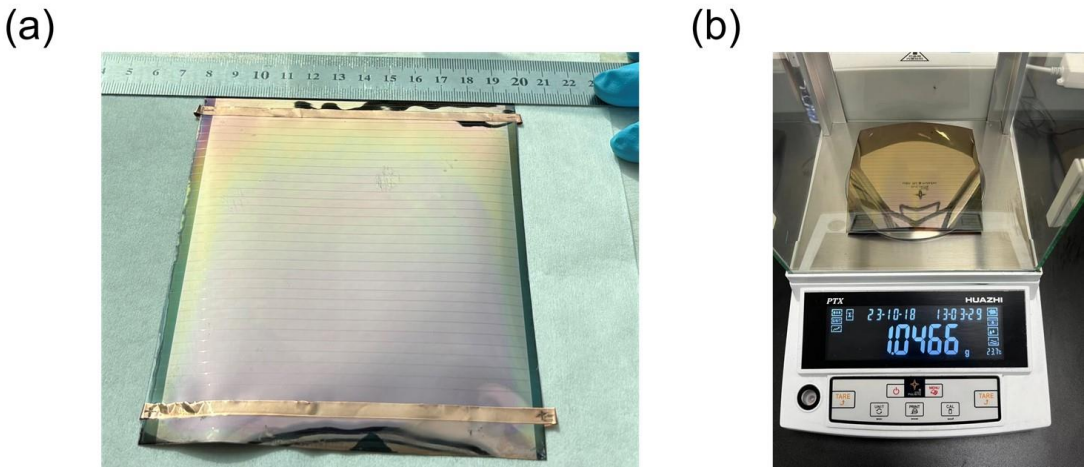


**Figure S6.** (a) Photograph of flexible perovskite solar module. (b) Self-tested weighting results of flexible solar module.

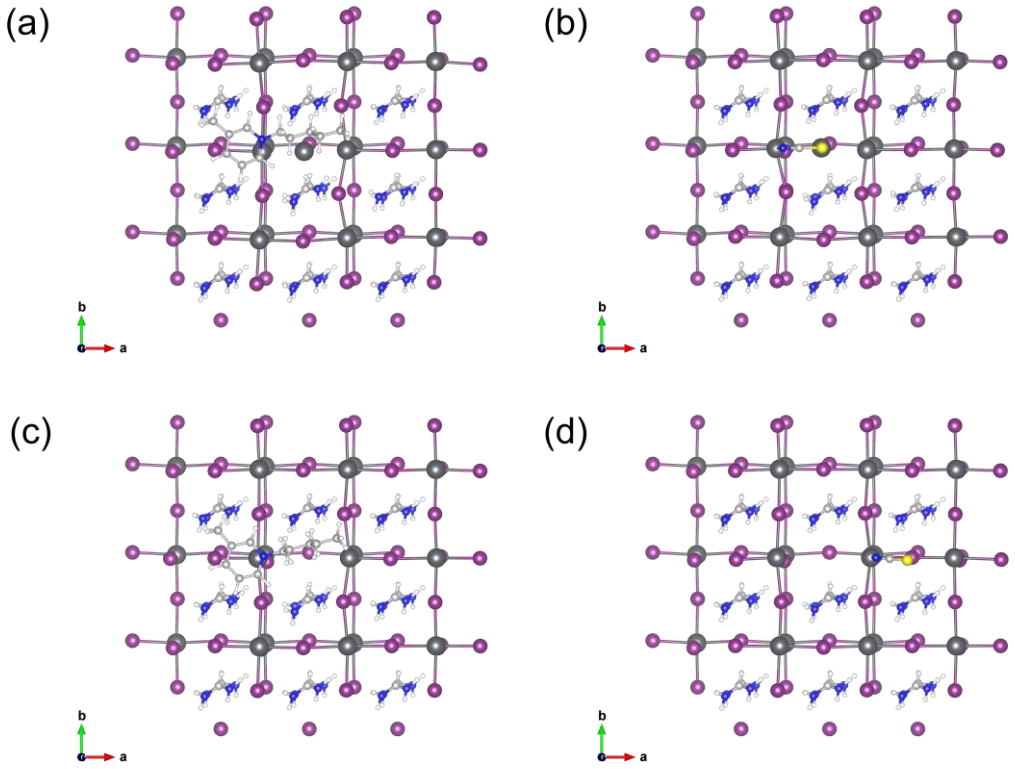


**Figure S7.** (a-b) Theoretical structures of $BPy^+$ (a) and $SCN^-$ (b) adsorbed on the $PbI_2$-terminated perovskite (100) plane with $Pb_I$ antisite defects. (c-d) Theoretical structure of $BPy^+$ (c) and $SCN^-$ (d) adsorbed on the $PbI_2$-terminated perovskite (100) plane with $V_I$ defects.

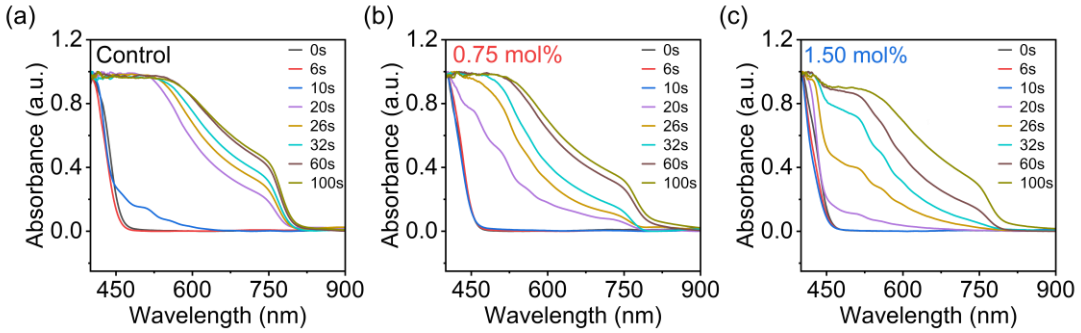


**Figure S8.** Evolution of the absorption spectra of perovskite films with the increased BPySCN concentrations from (a) 0 to (b) 0.75 and (c) 1.50 mol%.

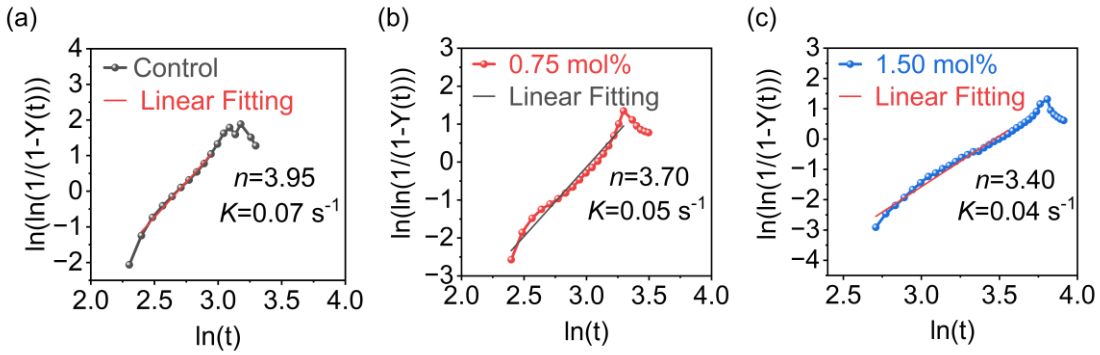


**Figure S9.** Linear fitting for the ln(-ln(1-Y(t))) versus ln(t) plot of perovskite films with the increased BPySCN concentrations from (a) 0 to (b) 0.75 and (c) 1.50 mol%. to determine the dimensionality (*n)* and rate constant (*K*).

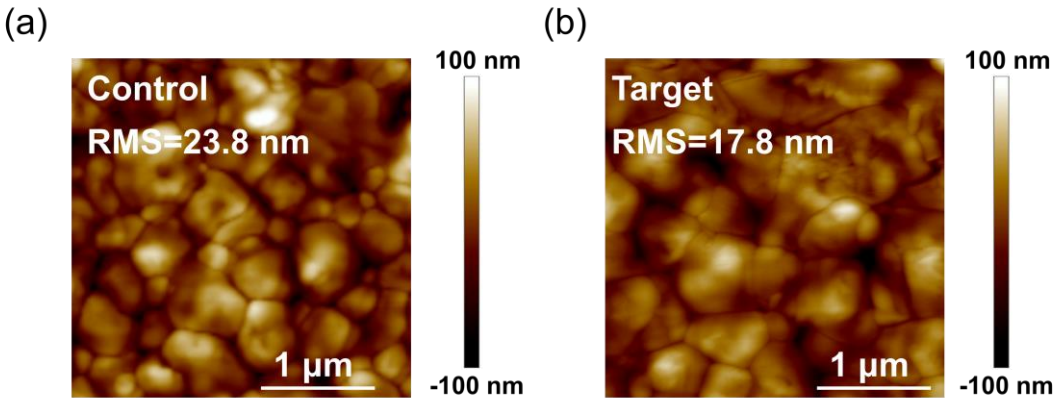


**Figure S10:** AFM topography images of the control (a) and target (b) films, showing the root-mean-square roughness (RMS).

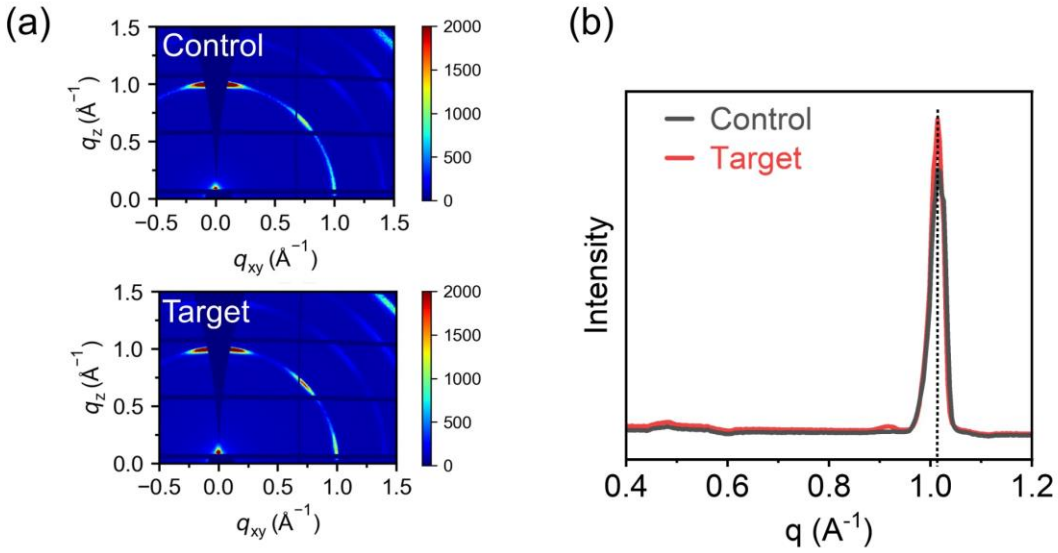


**Figure S11.** (a) 2D-GIWAXS patterns of control and target films and (b) corresponding line-cut profiles extracted from GIWAXS patterns.

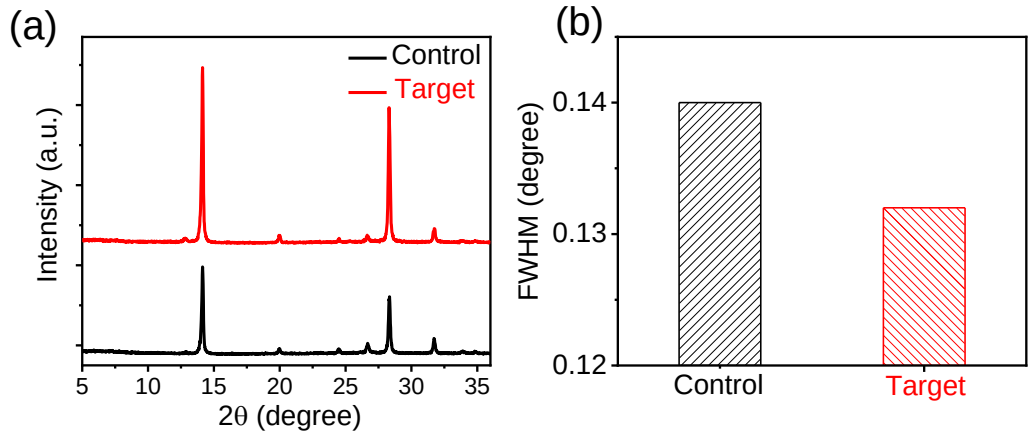


**Figure S12.** (a) XRD patterns and (b) FWHM values for different perovskite films.

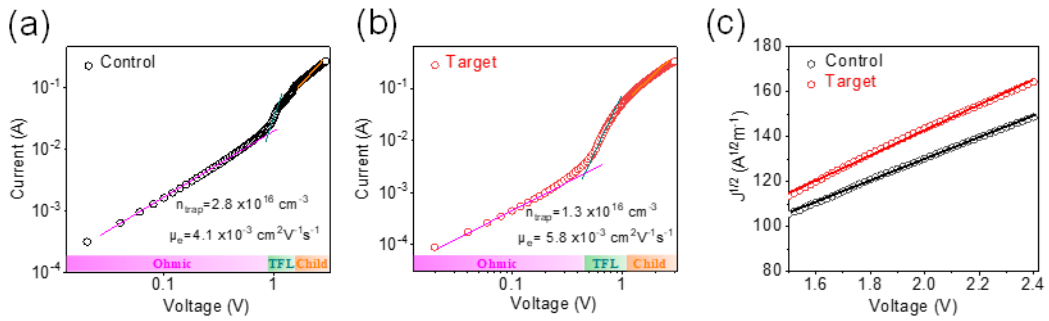


**Figure S13.** (a-b) Dark *I-V* behaviors of electron-only devices (ITO/$SnO_2$/perovskite/PCBM/Ag) showing different regimes as function of voltage bias. (c) The $J^{1/2}$ versus *V* plots extracted from the child region in dark *I-V* curves.

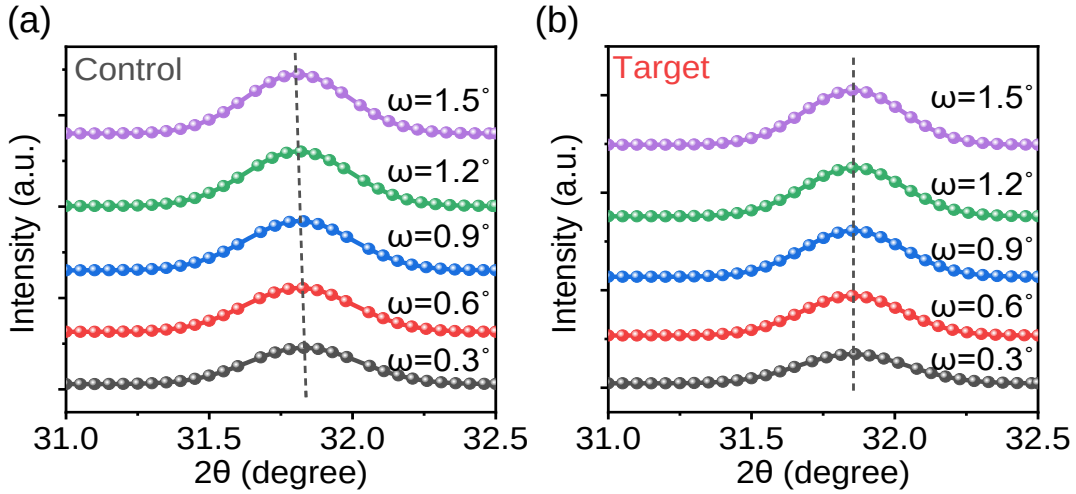


**Figure S14.** Line cuts of the GIXRD patterns of the control (a) and target (b) perovskite films.

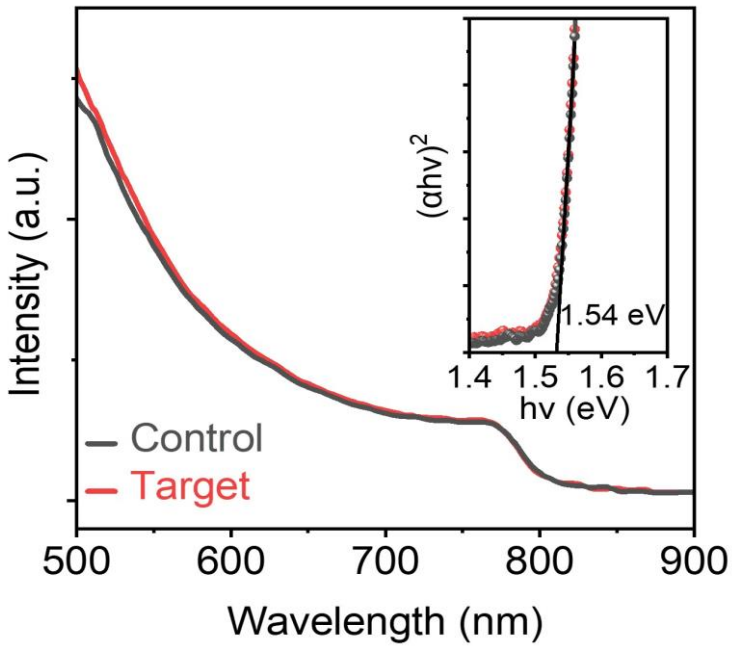


**Figure S15.** UV-vis absorption spectra of perovskite films with the corresponding Tauc plots shown inset.

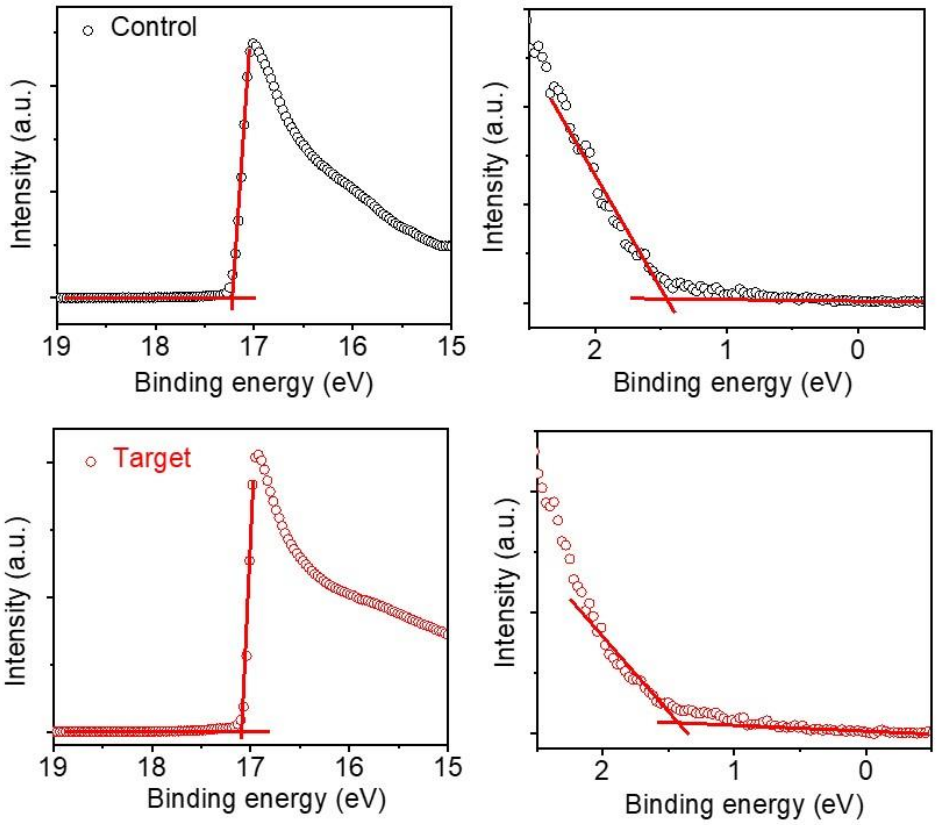


**Figure S16.** UPS spectra of control and target perovskite films, showing the (a) $E_{Cutoff}$ level and (b) the value of $E_{Fermi\ edge}$.

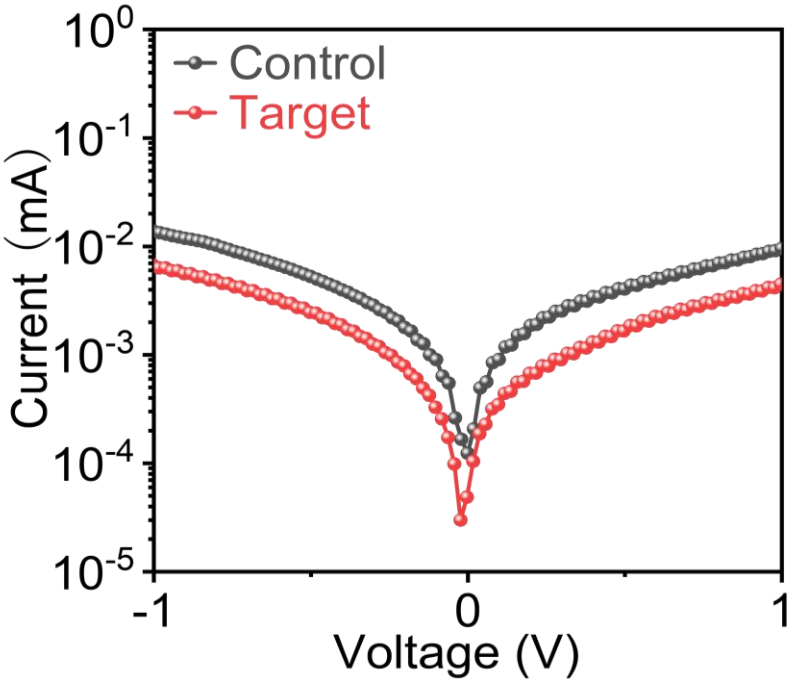


**Figure S17**. Dark *I–V* curves for the control and target devices.

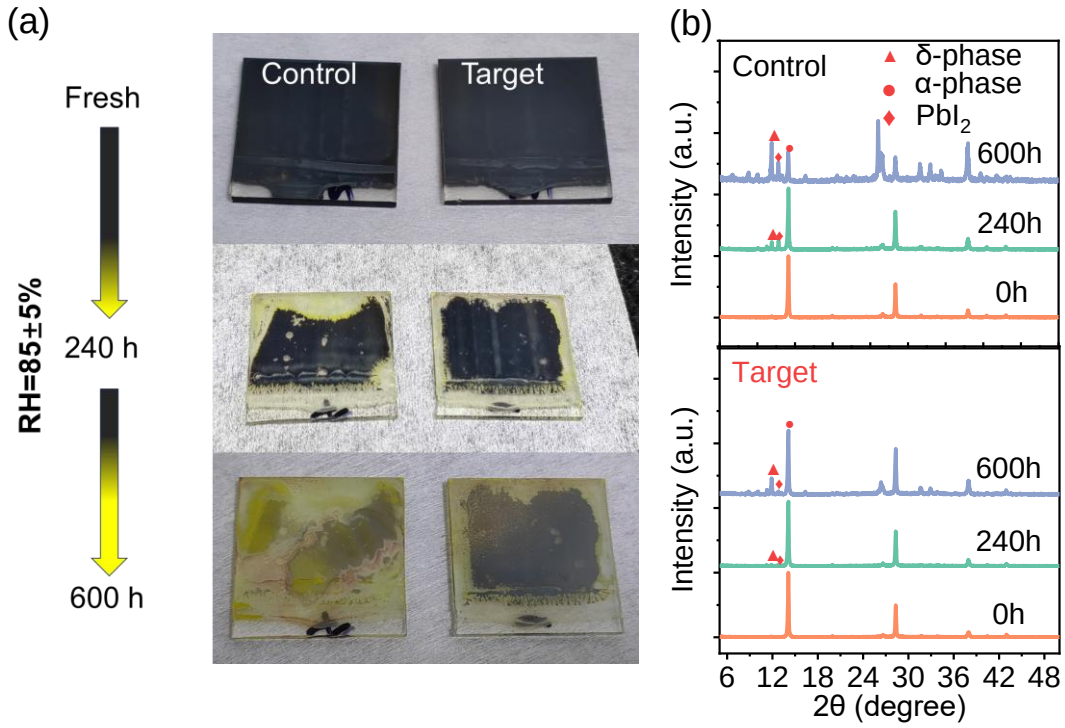


**Figure S18.** Photographs (a) and XRD patterns (b) of the control and target perovskite films as function of aging time under ambient conditions at 85±5% relative humidity.

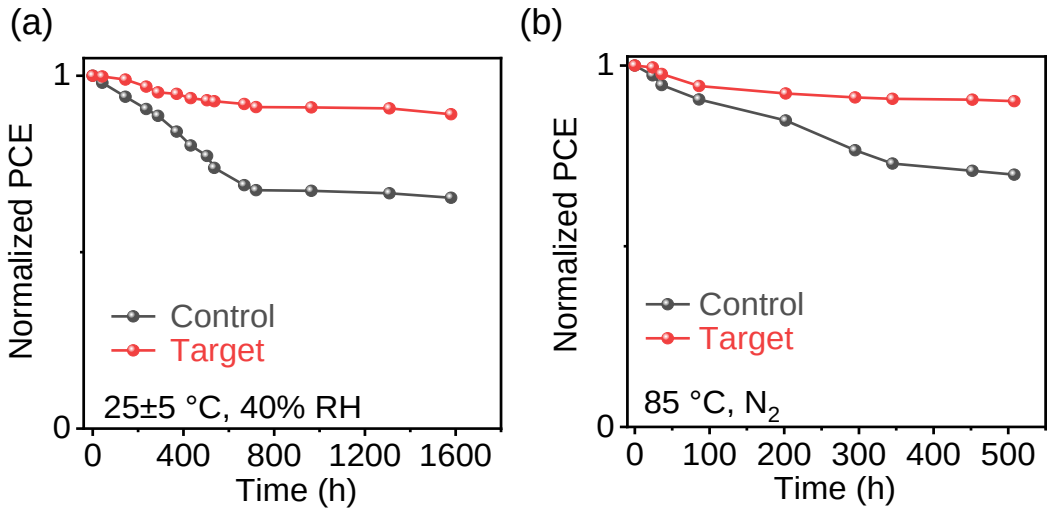


**Figure S19.** (a) Comparison of environmental stability of the unencapsulated flexible PSCs exposed to the ambient environment with ca. 40% humidity at room temperature. (b) Comparison of thermal stability of unencapsulated flexible PSCs under continuous 85 °C heating in $N_2$ atmosphere.

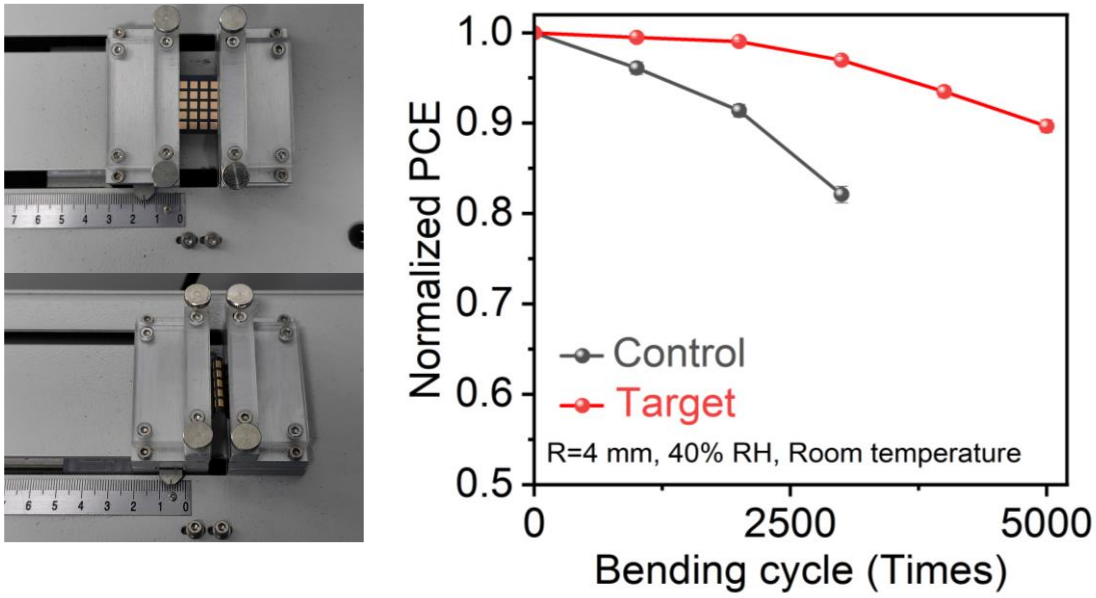


**Figure S20.** Comparison of mechanical stability of the unencapsulated F-PSCs under multiple-cycle bending test with a curvature radius (R) of 4 mm in air condition (ca. 40% humidity and room temperature).

**Table S1**. Summary of the photovoltaic parameters of rigid PSCs under different BPySCN incorporation concentrations.

| | $V_{oc}$ (V) | $J_{sc}$ (mA $cm^{-2}$) | FF (%) | PCE (%) |
|---|---|---|---|---|
| Control | 1.16 | 25.05 | 73.3 | 21.27 |
| 0.45 mol % | 1.17 | 25.11 | 78.8 | 23.12 |
| 0.75 mol % | 1.18 | 25.14 | 80.1 | 23.70 |
| 1.05 mol % | 1.17 | 25.22 | 75.4 | 22.34 |
| 1.50 mol% | 1.14 | 25.19 | 74.1 | 21.25 |

**Table S2.** Photovoltaic parameters and hysteresis index for the rigid PSCs.

| | Scanning mode | $V_{oc}$ (V) | $J_{sc}$ (mA $cm^{-2}$) | FF (%) | PCE (%) | Hysteresis Index (%) |
|---|---|---|---|---|---|---|
| Control | Reverse | 1.14 | 25.08 | 73.8 | 21.26 | 3.3 |
| | Forward | 1.12 | 25.05 | 72.5 | 20.57 | |
| Target | Reverse | 1.18 | 25.14 | 80.1 | 23.70 | 1.3 |
| | Forward | 1.16 | 25.21 | 79.8 | 23.40 | |

**Table S3.** Photovoltaic parameters for the control and target F-PSCs.

| F-PSCs | $V_{oc}$ (V) | $J_{sc}$ (mA $cm^{-2}$) | FF (%) | PCE (%) |
|---|---|---|---|---|
| Control | 1.13 | 24.53 | 75.7 | 20.98 |
| Target | 1.16 | 24.85 | 79.9 | 23.01 |

**Table S4.** Photovoltaic parameters for the flexible perovskite solar module.

| Flexible solar modules | $V_{oc}$ (V) | $J_{sc}$ (mA $cm^{-2}$) | FF (%) | PCE (%) | Pmax (mW) | Active area ($cm^2$) | Power density (W/kg) |
|---|---|---|---|---|---|---|---|
| Self-tested | 32.49 | 0.69 | 78.5 | 17.52 | 2061.7 | 117.7 | 1969.1 |
| Certified | 31.82 | 0.69 | 71.8 | 15.30 | 1790.6 | 117.0 | 1705.3 |

**Table S5**. Summary of the specific power and corresponding active area of flexible solar cells technologies.

| Photovolatic technology | Specific power ($W\ g^{-1}$) | Active area ($cm^2$) | Reference |
|---|---|---|---|
| F-PSCs | 1.96 | 0.1 | 4 |
| F-PSCs | 4.16 | 0.09 | 5 |
| F-PSCs | 23.26 | 0.06 | 6 |
| F-PSCs | 26.9 | 0.1 | 7 |
| F-PSCs | 29.4 | 0.17 | 8 |
| F-PSCs | 23 | 1 | 9 |
| F-PSCs | 35 | 1 | 10 |
| Flexible silicon solar module | 1.9 | 274.4 | 11 |
| Flexible perovskite solar module | 1.97 | 117.7 | **This work** |

**Table S6.** Fitting parameters for TRPL spectra of different perovskite films.

| | $A_1$ | $\tau_1$ (ns) | $A_2$ | $\tau_2$ (ns) | $\tau_{ave}$ (ns) |
|---|---|---|---|---|---|
| Control | 83.3% | 382.8 | 16.7% | 90.1 | 333.8 |
| Target | 56.0% | 860.0 | 44.0% | 242.2 | 588.0 |

**Table S7.** Summaries of series resistance ($R_s$), transport resistance ($R_{tr}$) and recombination resistance ($R_{rec}$) obtained from electrical impedance spectroscopy (EIS) for different devices.

| | $R_s$ (Ω) | $R_{tr}$ (Ω) | $R_{rec}$ (Ω) | $C_{tr}$ ($F\ cm^{-2}$) | $C_{rec}$ ($F\ cm^{-2}$) |
|---|---|---|---|---|---|
| Control | 46.3 | 546.3 | 3268.1 | $1.33\times10^{-8}$ | $1.68\times10^{-8}$ |
| Target | 21.8 | 533.2 | 7791.0 | $2.97\times10^{-8}$ | $1.16\times10^{-8}$ |

**Reference:**


1. G. Kresse, J. Furthmüller, *Computational Materials Science* 1996, *6*, 15.
2. G. Kresse, D. Joubert, *Phys. Rev. B* 1999, 59, 1758.
3. S. Grimme, J. Antony, S. Ehrlich, H. Krieg, *The Journal of Chemical Physics* 2010, 132, 154104.
4. Y. Li, L. Meng, Y. Yang, G. Xu, Z. Hong, Q. Chen, J. You, G. Li, Y. Yang, Y. Li, *Nat Commun.* 2016, 7, 10214.
5. M. Xie, J. Wang, J. Kang, L. Zhang, X. Sun, K. Han, Q. Luo, J. Lin, L. Shi, C.-Q. Ma, *Flex. Print. Electron.* 2019, 4, 034002.
6. H. Zhang, J. Cheng, D. Li, F. Lin, J. Mao, C. Liang, A. K.-Y. Jen, M. Grätzel, W. C. H. Choy, *Adv. Mater.* 2017, 29, 1604695.
7. Q. Wang, C.-C. Chueh, T. Zhao, J. Cheng, M. Eslamian, W. C. H. Choy, A. K.-Y. Jen, *ChemSusChem* 2017, 10, 3794.
8. S. Kang, J. Jeong, S. Cho, Y. J. Yoon, S. Park, S. Lim, J. Y. Kim, H. Ko, *J. Mater. Chem. A* 2019, 7, 1107.
9. B. Hailegnaw, S. Demchyshyn, C. Putz, L. E. Lehner, F. Mayr, D. Schiller, R. Pruckner, M. Cobet, D. Ziss, T. M. Krieger, A. Rastelli, N. S. Sariciftci, M. C. Scharber, M. Kaltenbrunner, *Nat Energy* 2024, 18, 379-387.
10. M. Kaltenbrunner, G. Adam, E. D. Głowacki, M. Drack, R. Schwödiauer, L. Leonat, D. H. Apaydin, H. Groiss, M. C. Scharber, M. S. White, N. S. Sariciftci, S. Bauer, *Nature Mater* 2015, 14, 1032.
11. Y. Li, X. Ru, M. Yang, Y. Zheng, S. Yin, C. Hong, F. Peng, M. Qu, C. Xue, J. Lu, L. Fang, C. Su, D. Chen, J. Xu, C. Yan, Z. Li, X. Xu, Z. Shao, *Nature* 2024, 626, 105.